ORIGINAL ARTICLE

Spatial distribution of turbulent diapycnal mixing along the Mindanao current inferred from rapid-sampling Argo floats

Ying He[1,3] · Jianing Wang[1,2,3] · Fan Wang[1,2,3] · Toshiyuki Hibiya[4]

Abstract

The Mindanao Current (MC) bridges the North Pacific low-latitude western boundary current system region and the Indonesian Seas by supplying the North Pacific waters to the Indonesian Throughflow. Although the previous study speculated that the diapycnal mixing along the MC might be strong on the basis of the water mass analysis of the gridded climatologic dataset, the real spatial distribution of diapycnal mixing along the MC has remained to be clarified. We tackle this question here by applying a finescale parameterization to temperature and salinity profiles obtained using two rapid-sampling profiling Argo floats that drifted along the MC. The western boundary (WB) region close to the Mindanao Islands and the Sangihe Strait are the two mixing hotspots along the MC, with energy dissipation rate ε and diapycnal diffusivity K_ρ enhanced up to $\sim 10^{-6}$ W kg^{-1} and $\sim 10^{-3}$ m^2 s^{-1}, respectively. Except for the above two mixing hotspots, the turbulent mixing along the MC is mostly weak, with ε and K_ρ to be 10^{-11}–10^{-9} W kg^{-1} and 10^{-6}–10^{-5} m^2 s^{-1}, respectively. Strong mixing in the Sangihe Strait can be basically attributed to the existence of internal tides, whereas strong mixing in the WB region suggests the existence of internal lee waves. We also find that water mass transformation along the MC mainly occurs in the Sangihe Strait where the water masses are subjected to strong turbulent mixing during a long residence time.

Keywords Turbulent diapycnal mixing · Mindanao current · Indonesian throughflow · Water mass transformation · Internal tides · Internal lee waves

1 Introduction

The Mindanao Current (MC) is an important part of the North Pacific low-latitude western boundary current system (NP-LLWBC; see Fig. 1). The MC originates from the southward bifurcation of North Equatorial Current (NEC) near the Philippine coast and transports the North Pacific Tropical Water (NPTW) and North Pacific Intermediate Water (NPIW) toward the equator. Upon reaching the southern tip of the Mindanao Islands near 5° N, part of the MC intrudes westward into the Sulawesi Sea, supplying source waters of the Indonesian Throughflow (ITF), with the remaining portion flowing eastward through the Mindanao Retroflection to feed the North Equatorial Countercurrent (NECC) (e.g., Hu et al. 2015; Kashino et al. 2001; Lukas et al. 1996). Underneath the MC, there exists the Mindanao Undercurrent (MUC) with a mean northward velocity (Hu et al. 1991).

The MC bridges the NP-LLWBC region and the Indonesian Seas by supplying the North Pacific waters to the ITF (e.g., Hu et al. 2015; Kashino et al. 2001), and hence the water mass transformation along the MC can influence the properties of the ITF's source waters. On the basis of the water mass analysis using the gridded climatologic data from World Ocean Database 2009 and Argo floats, Li and Wang (2012) speculated the significant decrease of the salinity of NPTW along the MC caused by the existence of enhanced turbulent mixing along the MC.

✉ Jianing Wang
wjn@qdio.ac.cn

✉ Fan Wang
fwang@qdio.ac.cn

[1] Key Laboratory of Ocean Circulation and Waves, Institute of Oceanology, Center for Ocean Mega-Science, Chinese Academy of Sciences, Qingdao, China

[2] Laboratory for Ocean and Climate Dynamics, Pilot National Laboratory for Marine Science and Technology, Qingdao, China

[3] University of Chinese Academy of Sciences, Beijing, China

[4] Department of Earth and Planetary Science, Graduate School of Science, The University of Tokyo, Tokyo, Japan

Fig. 1 Schematic of the upper-ocean circulations and their carrying water masses in the North Pacific low-latitude western boundary current system (NP-LLWBC). The routes of the MC, MUC, and other circulations are depicted by red solid, red dashed, and black solid arrow lines, respectively. *MC* Mindanao Current, *MUC* Mindanao Undercurrent, *KC* Kuroshio Current, *NEC* North Equatorial Current, *NECC* North Equatorial Countercurrent, *NGCUC* New Guinea Coastal Undercurrent, *NPTW* North Pacific Tropical Water, *NPIW* North Pacific Intermediate Water, *SPTW* South Pacific Tropical Water, *AAIW* Antarctic Intermediate Water. The bathymetry is from Smith and Sandwell ([1997](#), same hereinafter) (color figure online)
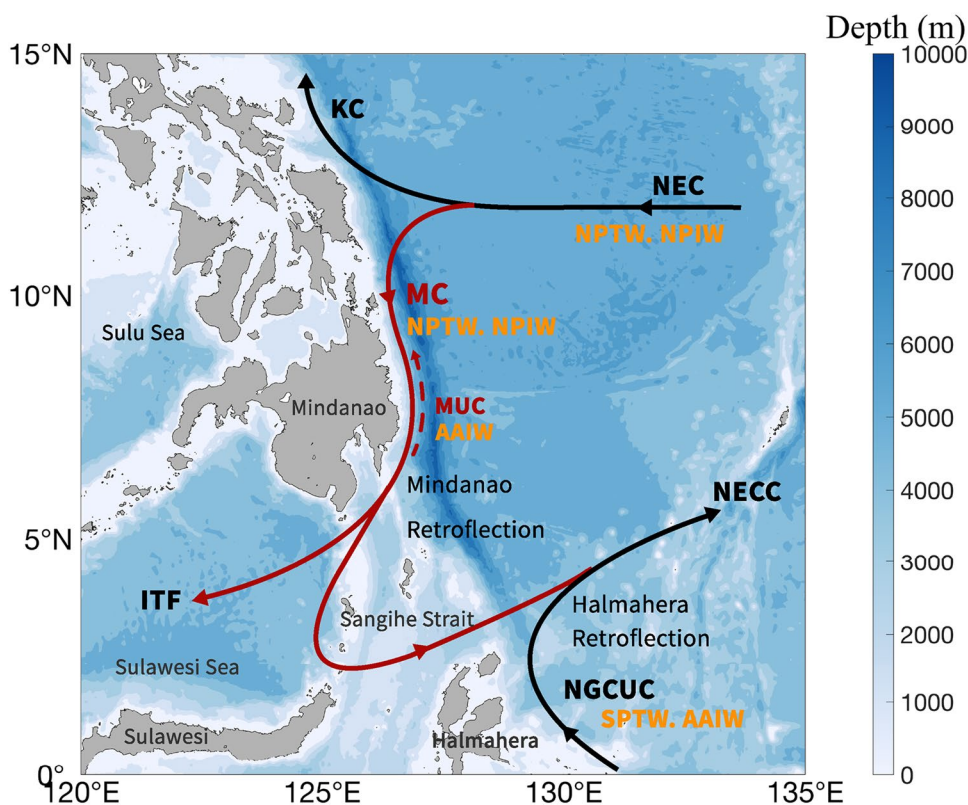
Some mixing related studies have been carried out in the NP-LLWBC region and the Indonesian Seas. For the NP-LLWBC region, on the basis of finescale parameterization applied to conductivity-temperature-depth (CTD) profiles, Yang et al. ([2014](#)) found that the diapycnal diffusivity K_ρ in the NP-LLWBC region can reach up to $\sim 10^{-2}$ m^2 s^{-1}, associated with strong shear of the Kuroshio and the Mindanao Eddy. Liu et al. ([2017](#)), on the other hand, made the first direct microstructure measurements of turbulent mixing in the NP-LLWBC region, categorizing it as a weak mixing regime with $K_\rho \sim 10^{-6}$ m^2 s^{-1}. For the Indonesian Seas, the numerical studies (e.g., Koch-Larrouy et al. [2007](#); Nagai and Hibiya [2015](#); Nagai et al. [2017](#)) and observational studies (e.g., Koch-Larrouy et al. [2015](#); Nagai et al. [2021](#)) both show that a large amount of tidal energy is available for strong diapycnal mixing in the Indonesian Seas, and the water masses transported by the ITF are significantly transformed by such strong turbulent mixing. Nevertheless, none of the above studies has paid much attention to the diapycnal mixing along the MC.

The previous speculation about the enhanced mixing along the MC and the lack of mixing research along the MC motivate us to clarify the spatial distribution of turbulent mixing along the MC. During a cruise in 2016, we deployed an Argo Float (No. 0761) in the NP-LLWBC region, which was set to work at the highest sampling frequency. Fortunately, this float and another Argo Float (No. 2902729)

drifted along the MC' routes, providing us an opportunity to examine the turbulent mixing and water mass transformation along the MC.

The present paper is organized as follows. Section [2](#) describes the data and methods. Section [3](#) presents the spatial distribution of turbulent mixing along the MC, and discusses the energy sources for the enhanced mixing and the water mass transformation along the MC. A summary is given in Sect. [4](#).

## 2 Data and methods

2.1 Argo float measurement

The NAVIS Argo Float 0761 was deployed at 130° E, 8.6° N on December 23, 2016, and returned the last profile at 128.2° E, 5.1° N on July 18, 2017. This float, equipped with SBE 41CP sensors, collected a total of 348 profiles. The working procedure for one profile cycle includes five steps: (1) descending from the surface to a drifting depth of 1000 m, (2) drifting at a depth of 1000 m, (3) further descending to a depth of 2000 m; (4) ascending from a depth of 2000 m to the surface, (5) transmitting data using the Iridium satellite, each of which takes approximately 4, 0.2, 3, 6, and 0.5 h. During its ascending period, temperature, salinity, and pressure data were collected at 2 m intervals. We set the drifting

time at 1000 m depth to 12 min instead of the often-used 9 days, making this float a rapid-sampling Argo float with an average horizontal resolution of ~ 4.69 km.

The APEX Argo Float 2902729 was deployed at 130.5° E, 14.9° N on April 19, 2018, and returned the last profile at 122.6° E, 3.1° N on January 2, 2020. The float was equipped with SBE 41 sensors and collected a total of 339 profiles. During its ascending period, temperature, salinity, and pressure data were collected at 2 m intervals over the upper 1000 m depth and at 10 m intervals over the depth range of 1000–2000 m. The profiling time varied depending on the different regions (Fig. 2b): 5 days for the first 15 profiles along the NEC from 130.5 to 124.7° E (black dots), 17.8 h for the following 27 profiles along the western boundary (WB) from 8.8 to 3.1° N (orange

dots) and the 175 profiles in the Sangihe Strait (magenta dots), 54.4 h for the following 122 profiles in the Sulawesi Sea (cyan dots). Note that no Argo float data was available from 25 June to 29 October 2018, namely, after the last profile of the NEC region and before the first profile of the WB region (Fig. 2b). The procedure made this float also a rapid-sampling Argo float along the MC route with an average horizontal resolution of ~ 11.53 km.

Furthermore, we picked out 2712 Argo profiles during a period of May 1998 to May 2020 when all of the following criteria were satisfied (Fig. 2c): (1) the location within 120° E–131° E and 0°–15° N, (2) quality rating of "A" (i.e., the profile containing 100% good values), (3) measurement depth deeper than 500 m, and (4) vertical sampling interval smaller than 2.2 m.
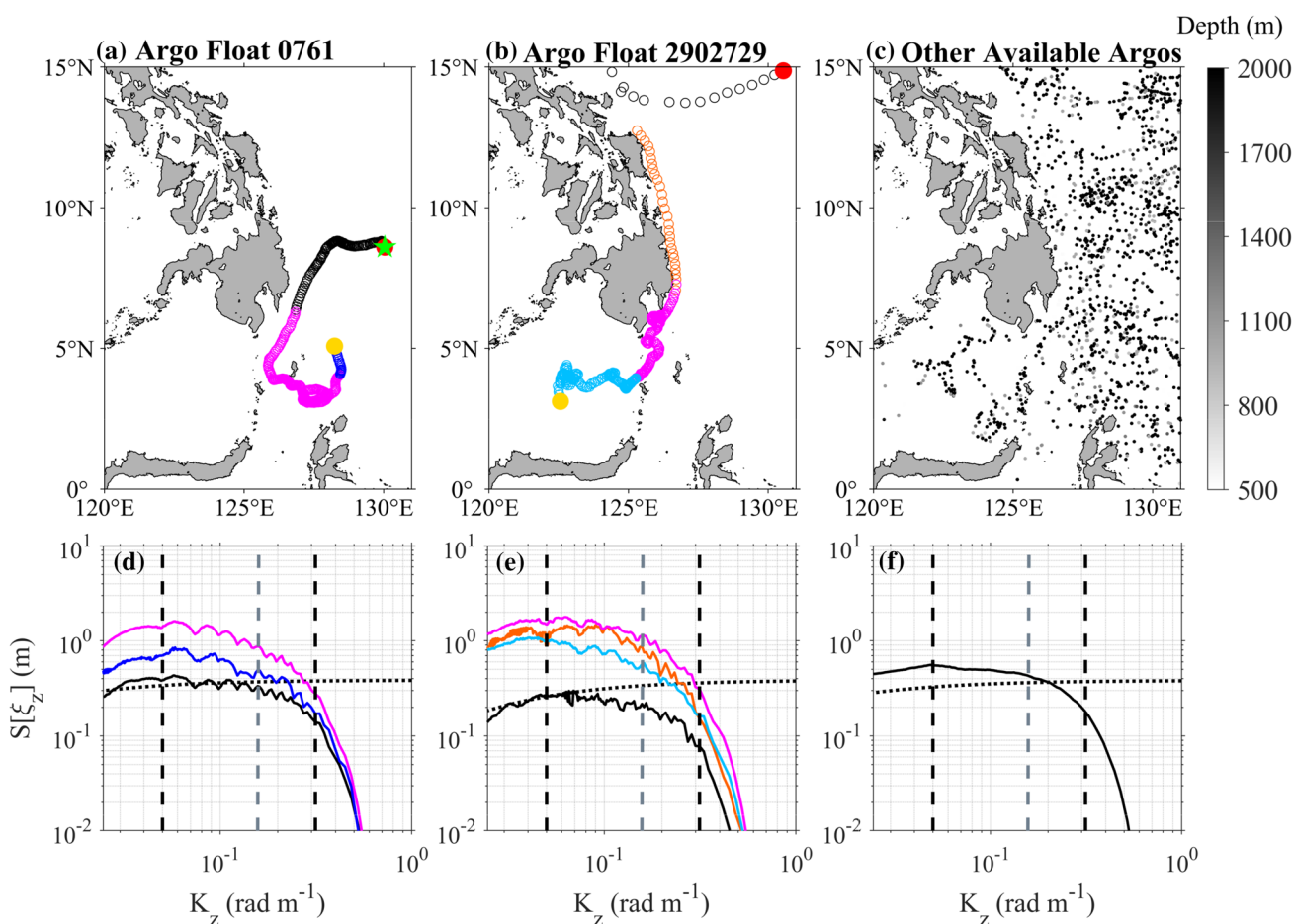
Fig. 2 The trajectories (top) and observed strain spectra (bottom) for Argo Floats (**a**, **d**) 0761 and (**b**, **e**) 2902729 with black, orange, magenta, dark blue, and light blue circles denoting the profiles in the NEC region, the western boundary (WB) region, the Sangihe Strait, the NGCUC region and the Sulawesi Sea, respectively. The first and last observed profiles are highlighted with a red and yellow dot, respectively. **c** The locations and **f** observed stain spectra for other available Argo profiles used in this study with the color denoting the maximum measurement depth. In **d**–**f**, the GM strain spectra are depicted by black dotted lines for reference, and the minimum wavenumber and the maximum wavenumber range for integration are denoted by black and gray dashed lines, respectively (see text) (color figure online)

2.2 Finescale parameterization

To estimate turbulent dissipation rates, the strain-based finescale parameterization were applied to temperature and salinity data (e.g., Kunze et al. 2006; Whalen et al. 2015). This method assumes that the turbulent dissipation results from a downscale energy transfer associated with internal wave–wave interactions (e.g., Kunze et al. 2006; Polzin et al. 2014). The formulated turbulent kinetic energy dissipation rate ε is

$$\varepsilon = \varepsilon_0 \left(\frac{N^2}{N_0^2} \right) \frac{\langle \xi_z^2 \rangle^2}{\langle \xi_{zGM}^2 \rangle^2} h(R_\omega) j(f, N), \tag{1}$$

with

$$h(R_\omega) = \frac{1}{6\sqrt{2}} \frac{R_\omega (R_\omega + 1)}{\sqrt{R_\omega - 1}}, \tag{2}$$

and

$$j(f, N) = \frac{f \cdot \cosh^{-1}(N/f)}{f_{30} \cdot \cosh^{-1}(N_0/f_{30})}, \tag{3}$$

where N^2 is the squared buoyancy frequency, $\langle \xi_z^2 \rangle^2$ and $\langle \xi_{zGM}^2 \rangle^2$ are the strain variances from the observations and GM76 model (Cairns and Williams 1976), respectively, angle bracket denotes variance integrated over a specified vertical wavenumber range, $j(f, N)$ is a latitudinal correction, R_ω represents the ratio of shear to strain variances, f and f_{30} represent the local Coriolis frequency and the Coriolis frequency at 30°, respectively, $\varepsilon_0 = 6.73 \times 10^{-10}$ m^2 s^{-2}, and $N_0 = 5.24 \times 10^{-3}$ s^{-1}. Since no shear data was available in our field observations, we adopted a fixed value $R_\omega = 7$. Actually, on the basis of the historical LADCP and CTD data, Kunze et al. (2006) found that the average R_ω in the Pacific equals to 7 ± 1 above 2000 m depth, which has been widely assumed in the previous similar studies in the Pacific Ocean (e.g., Li and Xu 2014; Zhu and Zhang 2018).

The dissipation rate was calculated for a sliding 256 m segment with a sequential increment of its center point depth by 16 m and a vertical resolution of 2 m. First, we calculated the strain in each segment using

$$\xi_z = \frac{N^2 - N_{ref}^2}{N_{ref}^2}. \tag{4}$$

Since not all vertical structures of the N^2 segments are quadratic or linear, we used a 128-point sliding average over N^2 profiles to calculate the N_{ref}^2 instead of a simple quadratic fit or linear fit of N^2 segments. Second, we obtained the spectrum $\varphi(k)$ through the Fourier transform and then integrated $\varphi(k)$ over a specified range of vertical wavenumber (k) as

$$\langle \xi_z^2 \rangle = \int_{k_{min}}^{k_{max}} \varphi_{(k)} dk, \tag{5}$$

where the minimum vertical wavenumber k_{min} was set to 1/125 cpm to avoid the longer wavelength contamination by the background stratification, and the maximum vertical wavenumber k_{max} was set to the value in a range of 1/40–1/20 cpm while satisfying $\langle \xi_z^2 \rangle \leq 0.2$ to avoid the underestimation of strain variance induced by oversaturation of the spectrum (Whalen et al. 2015) (the employed values of k_{min} and k_{max} are denoted in Fig. 2d–f). Third, the GM model strain variance was calculated over the same vertical wavenumber band mentioned above.

The diapycnal diffusivity K_ρ from the dissipation rate ε was obtained by

$$K_\rho = \Gamma \frac{\varepsilon}{N^2}, \tag{6}$$

where the conventional mixing efficiency $\Gamma = 0.2$ was used (Osborn 1980).

At the deployment location of Float 0761, a free-fall vertical microstructure profiler (VMP-500; manufactured by Rockland Scientific Inc.) was cast down to a depth of ~600 m. The VMP-500 was deployed about 9 h after Float 0761 started collecting data. Figure 3 shows the comparison between the two profiles of dissipation rates obtained from the finescale parameterization and the direct microstructure measurements. Although their magnitudes at the same depth are generally within an order of magnitude, a relatively larger discrepancy occurs at depths shallower than 250 m, and the distribution of ε from Argo generally follows that of peak ε from VMP-500 (Fig. 3). This suggests that the 256-m segment mean ε obtained from Argo data is generally reliable, although it may be overestimated when some large peak values exist in the segment.

It should be noted that, in the western boundary currents region, the finescale shear and strain variances might be contaminated by non-internal wave processes such as the strong mean shear. Liu et al. (2017) showed that the dissipation rates estimated from the strain-based finescale parameterizations tended to be overestimates, but that they were limited to one order of magnitude at most. Winkel et al. (2002) also suggested that the dissipation rates obtained from microstructure measurements can be mostly predicted using the shear-based finescale parameterizations within a factor of 2 along the Florida Current. Thus, the estimates from finescale strains can be regarded as a proxy for diapycnal mixing.
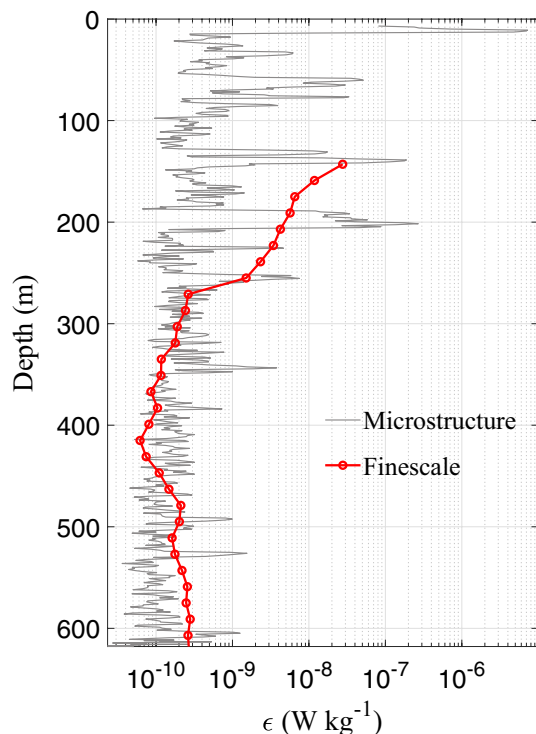
Fig. 3 Vertical profiles of the dissipation rate ε obtained from the finescale parameterization of Argo data (red) and the microstructure data (gray) at the deployment site of Argo Float 0761 (130° E, 8.6° N) on 23 December 2016 (color figure online)

3 Results and discussions

3.1 Spatial distributions of diapycnal mixing

The trajectories of the two Argo floats are shown in Fig. 2a and b, respectively. Argo Floats 0761 and 2902729 were both advected westward by the NEC along ~8.6° N and 15° N, respectively, and then southward by the MC. After reaching the Sangihe Strait, the two floats showed different pathways. Float 0761 turned anticlockwise and was finally directed northward by the New Guinea Coastal Undercurrent (NGCUC), while Float 2902729 was directed westward to the Sulawesi Sea by the ITF. The above two trajectories correspond well to the typical retroflection and penetration routes of the MC, respectively (Yuan et al. 2018).

Vertical profiles of ε, K_{ρ}, and N^2 along the trajectory of Float 0761 are shown in Fig. 4a, c, and e, respectively. In the NEC region, although the dissipation rate ε in the upper 200 m exceeds ~10^{-7} W kg^{-1}, it decreases down to 10^{-11}–10^{-9} W kg^{-1} at a depth of 500–1850 m. In the Sangihe Strait region, the dissipation rate over a depth of 200–1850 m becomes one to two orders of magnitude larger than that in the NEC region; the dissipation rate decreases from ~10^{-7} W kg^{-1} at 150 m depth to ~10^{-9} W kg^{-1} below 500 m depth. In the NGCUC region (128.2–128.5° E, 4–5°

N), the median value of ε is similar to that in the Sangihe Strait region over a depth of 150–500 m, but reduced down to a lower value similar to that in the NEC region over a depth of 500–1850 m.

The vertical distributions and values of N^2 in the above three regions are almost the same. The value of N^2 reaches 4×10^{-4} s^{-2} in the thermocline, and decreases from ~10^{-5} s^{-2} at 500 m depth to ~10^{-6} s^{-2} at 1850 m depth. The values of K_{ρ} over the depth range of 150–1850 m are mostly 10^{-6}–10^{-5} m^2 s^{-1} (background K_{ρ} values in the open ocean) in the NEC and NGCUC regions but increase up to ~10^{-3} m^2 s^{-1} in the Sangihe Strait especially around the seamounts.

Vertical profiles of ε, K_{ρ}, and N^2 along the trajectory of Float 2902729 are shown in Fig. 5a, c, and e, respectively. In the NEC region and Sangihe Strait, the vertical profiles and values of ε and K_{ρ} are similar to those from Float 0761, except for the value of K_{ρ} over a depth of 300–700 m. Compared to Float 0761, the weaker stratification during the measurement of Float 2902729 causes stronger K_{ρ} by two to three times. In the western boundary (WB) region, namely, the near-coastal area east of the Mindanao Islands, the values of ε and K_{ρ} are close to those in the Sangihe Strait over the depth ranges of 1000–1250 m and 1500–1850 m but are three to four times larger than those in the Sangihe Strait over the depth ranges of 300–1000 m and 1250–1500 m. In the Sulawesi Sea, the values of ε drop to 10^{-11}–10^{-8} W kg^{-1}, close to the situation in the NEC region, but the values of K_{ρ} become twice those in the NEC region because of the slightly weaker N^2.

The above analysis suggests that the mixing intensity significantly varies along the MC with mixing hotspots recognized in both of the WB region and the Sangihe Strait. Since the vertical profiles from two Argo floats are limited, we further explore the horizontal coverage of these two mixing hotspots by adding all the available Argo profiles in the NP-LLWBC region (120°–131° E, 0°–15° N).

Figure 6 shows the horizontal distributions of ε and K_{ρ} in the NP-LLWBC region, where the four main regions that two rapid-sampling Argo floats passed by are denoted by dashed black boxes (i.e., the WB region, NEC region, the Sulawesi Sea and the Sangihe Strait). The vertical profiles of median and 95% bootstrapped confidence intervals within the four main regions are shown in Fig. 7. At a depth of 150–500 m, the strongest turbulent mixing with ε of 10^{-9}–10^{-7} W kg^{-1} and K_{ρ} of 10^{-5}–10^{-4} m^2 s^{-1} occurs in the WB region close to the Mindanao Islands, while the second strongest turbulent mixing region with ε of 10^{-9}–10^{-7} W kg^{-1} and K_{ρ} of 10^{-5}–10^{-4} m^2 s^{-1} occurs in the Sangihe Strait. In the NEC region and the Sulawesi Sea, in contrast, turbulent mixing is generally weak with ε of 10^{-10}–10^{-7} W kg^{-1} and K_{ρ} of 10^{-6}–10^{-4} m^2 s^{-1}. At a depth of 500–1000 m, the values of ε in all of the above four regions decrease by one to two orders of magnitude. At a depth of 1000–1850 m, the mixing
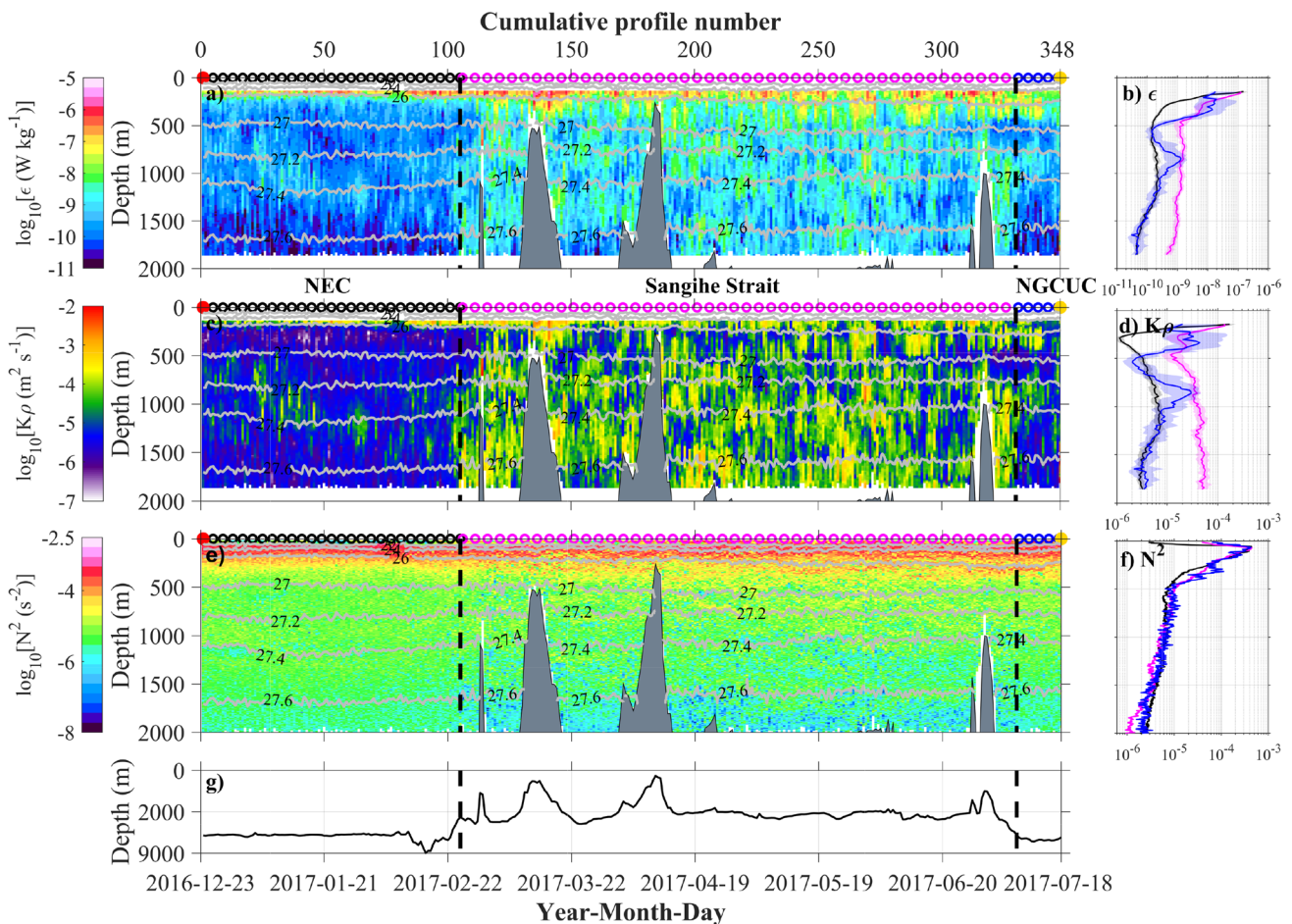
Fig. 4 Vertical profiles of **a** dissipation rate ε, **c** diapycnal diffusivity K_ρ, and **e** squared buoyancy frequency N^2 with contours of potential density σ_θ superimposed (light gray) along the trajectory of Argo Float 0761, and (**b**, **d**, **f**) their corresponding median profiles in the NEC region (black), Sangihe Strait (magenta), and NGCUC region (blue). Different regions are defined in Fig. 2a and are denoted by different color circles on the top x-axis in left panels and color lines in right panels. The bathymetry along the trajectory is depicted by black line in **g**, and by gray shadings in **a**–**c** (color figure online)

intensity further decreases down to the background level in the open ocean with ε of 10^{-11}–10^{-10} W kg^{-1} but for the WB region and the Sangihe Strait with ε of 10^{-10}–10^{-9} W kg^{-1}. In Fig. 6, we can see that strong mixing occurs throughout the Sangihe Strait, whereas that in the WB region is limited to a narrow area along the coast.

Next, we compare our results with the previous direct and indirect microstructure measurements in the same region. In the NEC region, our estimates of ε and K_ρ are close to those directly measured by Liu et al. (2017). Nagai et al. (2021) obtained the vertical profiles of ε and K_ρ using the VMP-X in the Sangihe Strait and the center of the Sulawesi Sea. Again, our estimates are consistent with their results. Unfortunately, there seem no direct microstructure measurements in the WB region. As an example of the indirect measurements through strain-based finescale parameterization, Yang et al. (2014) evaluated K_ρ within our WB and NEC regions to be one to three

orders of magnitude larger than our results with their strain spectra levels over the whole wavenumber range much higher than ours displayed in Fig. 2. Although the difference in the timing of observations is one of the possible reasons for this discrepancy, we believe that more reasonable explanation can be made by the different methods in calculating the strain; we used the squared buoyance frequency N^2, whereas Yang et al. (2014) used the potential temperature gradient θ_z. Actually, using θ_z to obtain the strain in the finescale parameterization, we confirm the resultant values of K_ρ over a depth of 250–1000 m are intensified by one to three orders of magnitude (Fig. 8). Since the NP-LLWBC region is the crossroad of water exchange between the northern and southern hemispheres (Fine et al. 1994), the thermohaline interleaving may cause the difference between θ_z and N^2, which must lead to the overestimates of diapycnal mixing (Kunze et al. 2006).
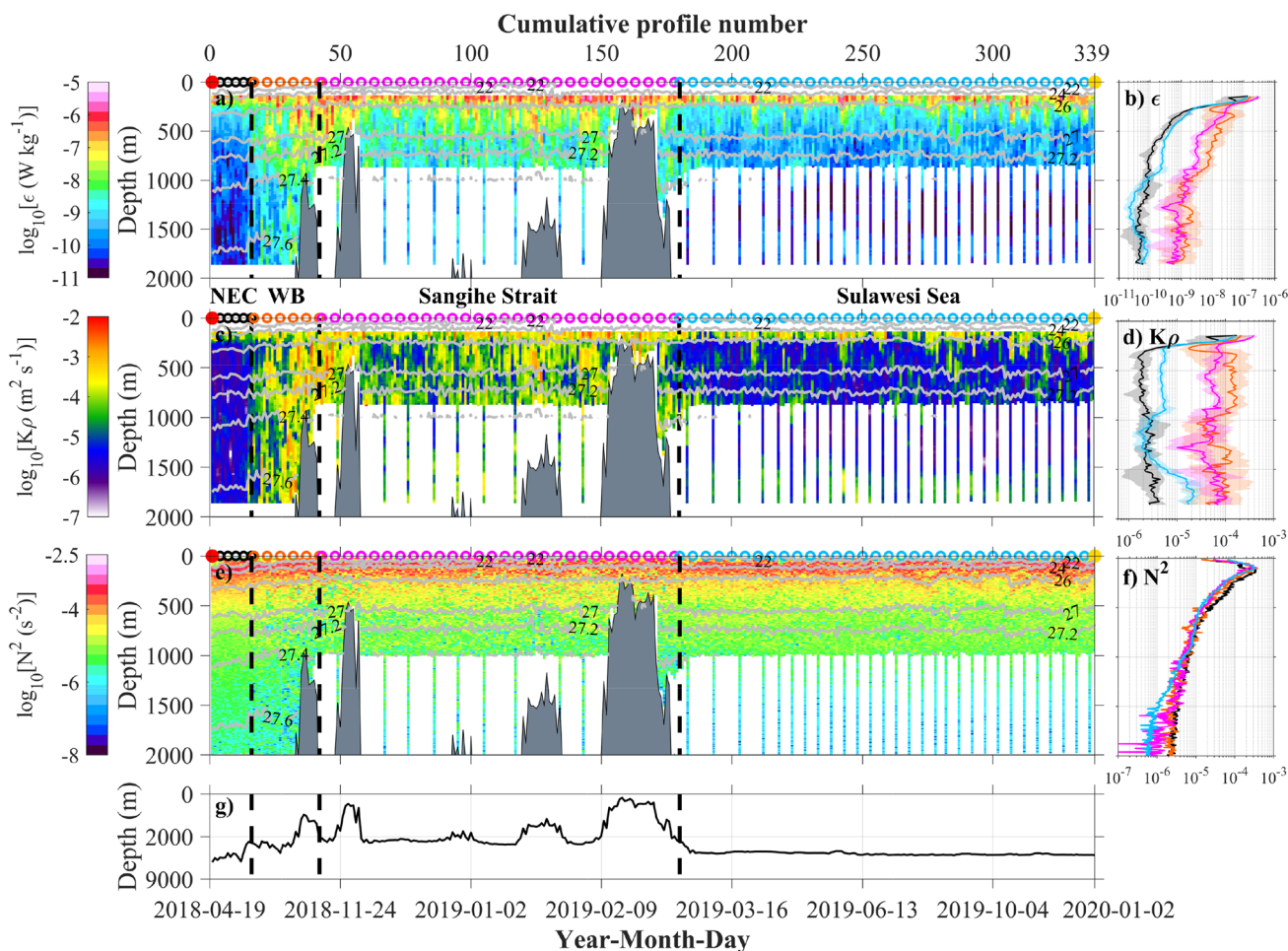
Fig. 5 As in Fig. 4 but for Argo Float 2902729

3.2 Major energy sources for the mixing hotspots

Internal tides and internal lee waves are the two main energy sources of the ocean interior mixing. The internal tides are excited by the barotropic tidal flow passing over rough topography. In contrast, the internal lee waves are generally excited by the deep geostrophic currents passing over the bottom topography. Such two kinds of waves can dissipate locally or remotely, transferring energy from tidal flow and sub-inertial flow to diapycnal mixing, respectively (Garrett and Kunze 2007; Sheen et al. 2013). The turbulent mixing induced by both internal waves can extend higher up off the ocean bottom (e.g., Hibiya et al. 2017; Kunze et al. 2006; Sheen et al. 2013).

Figures 9 and 10 show the variability of ε averaged over the depth range of 150–1850 m, the barotropic tidal flow speed, bottom roughness, water depth and wind stress along the trajectories of Float 0761 and Float 2902729, respectively. Here the bottom roughness is defined as the variance of the water depth over a rectangular box of $0.5° \times 0.5°$

centered at each grid based on the bathymetry data obtained from Smith and Sandwell (1997). The tidal flow speed is defined as the value averaged over 24 h just before the transmission of each Argo profile data to the satellite, which is obtained from the Oregon State University *TOPEX/Poseidon* solution (TPXO8-atlas data) with 1/30° resolution (Egbert and Erofeeva 2002). The wind stress along the trajectories of the two Argo floats is extracted from the daily wind stress data of Advanced SCATterometer (ASCAT) global wind dataset.

In general, energy dissipation rates are positively correlated with the tidal flow speed and the bottom roughness. Actually, the strong mixing areas in the Sangihe Strait benefit from large internal tides created by the combined effects of strong tidal flow and large bottom roughness, consistent with the previous numerical studies (Nagai and Hibiya 2015). Compared to the Sangihe Strait, profiles 77–105 of Float 0761 and profiles 7–16 of Float 2902729 in the NEC region also experience similar topography roughness, but the corresponding tidal flow is smaller, resulting in weak
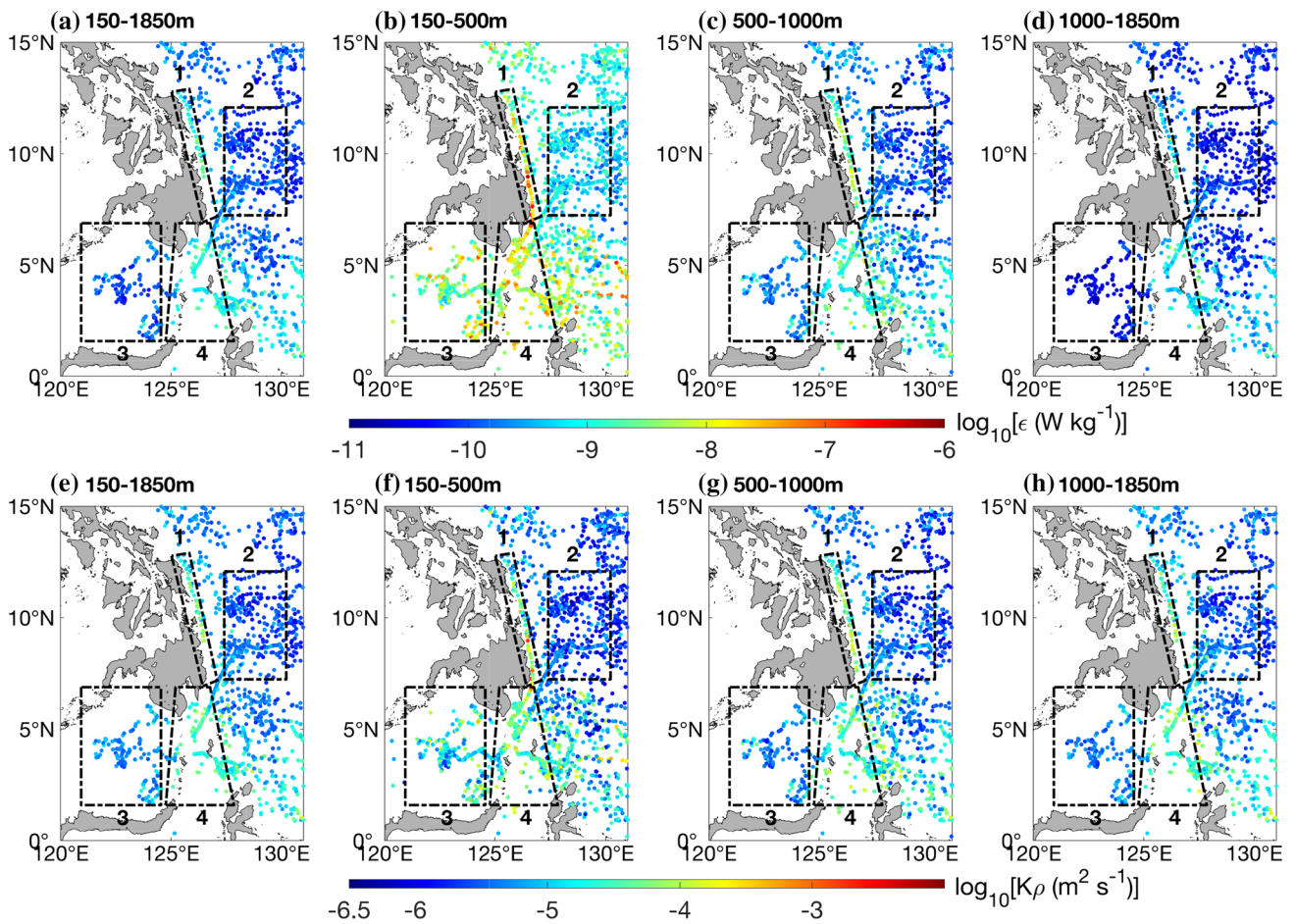
Fig. 6 Horizontal distributions of dissipation rate ε (top) and diapycnal diffusivity K_ρ (bottom) averaged over **a**, **e** 150–1850 m, **b**, **f** 150–500 m, **c**, **g** 500–1000 m, and **d**, **h** 1000–1850 m obtained from finescale parameterization of Argo data shown in Fig. 2a–c. Black dashed boxes denote four typical regions: the western boundary (WB) region (box1), the NEC region (box2), the Sulawesi Sea (box3) and the Sangihe Strait (box4)

Fig. 7 Vertical profiles of median **a** dissipation rate ε and **b** diapycnal diffusivity K_ρ (lines) and their 95% boot-strapped confidence intervals (shaded) in the four typical regions shown in Fig. 6, respectively
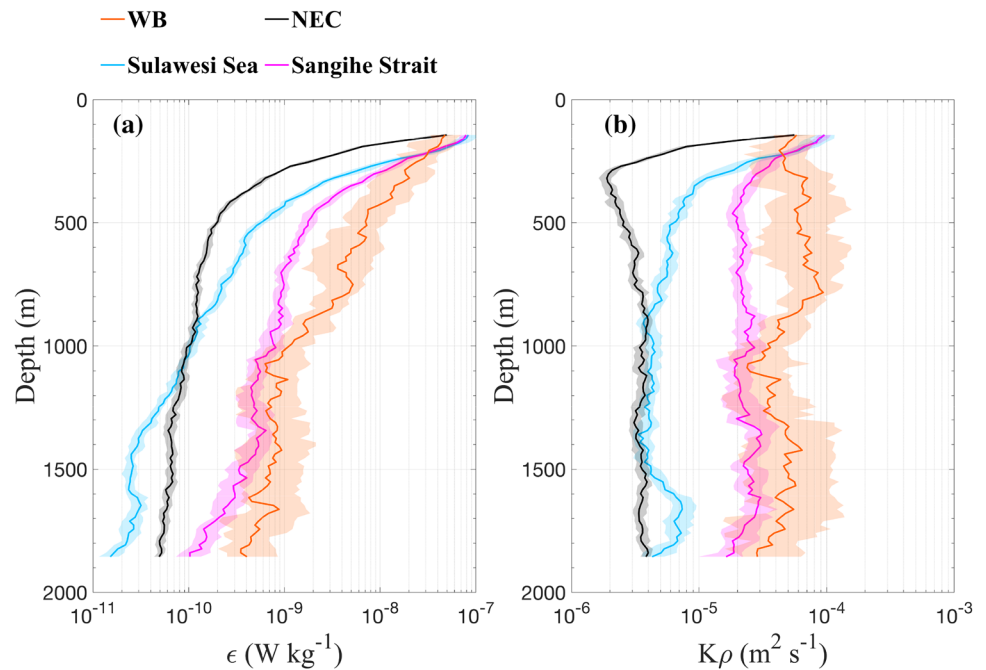
turbulent mixing with ε of ~ 10^{-10} W kg^{-1}. The values of ε in the Sulawesi Sea are in the range of 10^{-10}–10^{-9} W kg^{-1}, slightly higher than those in the NEC region, reflecting the fact that the tidal flow in the Sulawesi Sea is slightly stronger than that in the NEC region.

In the WB region, although tidal flow is very weak, the averaged dissipation rates are very large with ε higher than ~ 10^{-9} W kg^{-1}. The previous studies showed that the geostrophic flow speed can be 0.1–0.4 m s^{-1} even at ~ 2000 m depth off the east coast of the Philippines (Firing et al. 2005; Kashino et al. 2015), very close to the WB region. Thus, the WB region can be characterized by large bottom roughness and strong bottom-reaching geostrophic velocity, which makes it a possible generation site of internal lee waves providing lots of energy available for turbulent mixing.

We also check the possibility that wind energy input might contribute to the enhanced diapycnal mixing in the two mixing hotspots. However, the correlation coefficients R between the variations of wind stress and dissipation rate are − 0.02 for float 0761 and 0.12 for float 2902729 in the

Sangihe Strait and 0.13 for float 2902729 in the WB region, all too low to pass the significance test. This suggests that the wind energy input was not the primary contributor to the two mixing hotspots.

3.3 Water mass transformation

Float 2902729 went through the two mixing hotspots along the MC and finally entered the Indonesian Seas, providing us an opportunity to study the water mass transformation along the MC and the properties of the ITF's source waters. We classify the profiles obtained from Float 2902729 into seven stages depending on the locations to give potential temperature—salinity (θ–S) diagram for each (Fig. 11). Following Wang et al. (2016), the reference θ–S curves of the North Pacific water masses (at 15.5° N, 130.5° E) and South Pacific water masses (at 0°, 133° E) obtained from World Ocean Atlas 2013 (WOA13) annual climatology are also shown by thin black curves in Fig. 11. The variations of mean θ and S averaged over the isopycnals that characterize
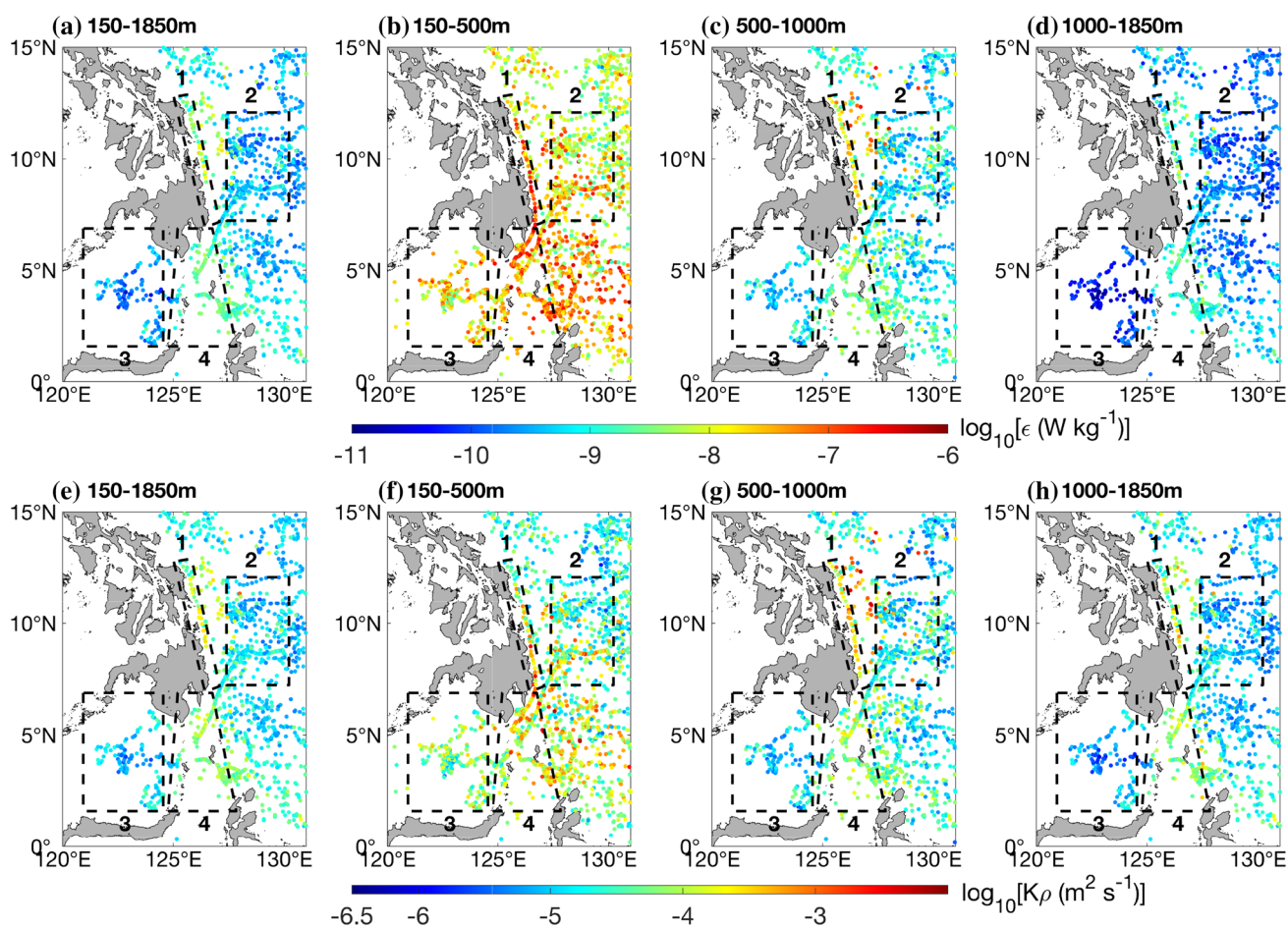
Fig. 8 As in Fig. 6, except that the strain is calculated using the potential temperature gradient θ_z instead of N^2 is incorporated into the finescale parameterization
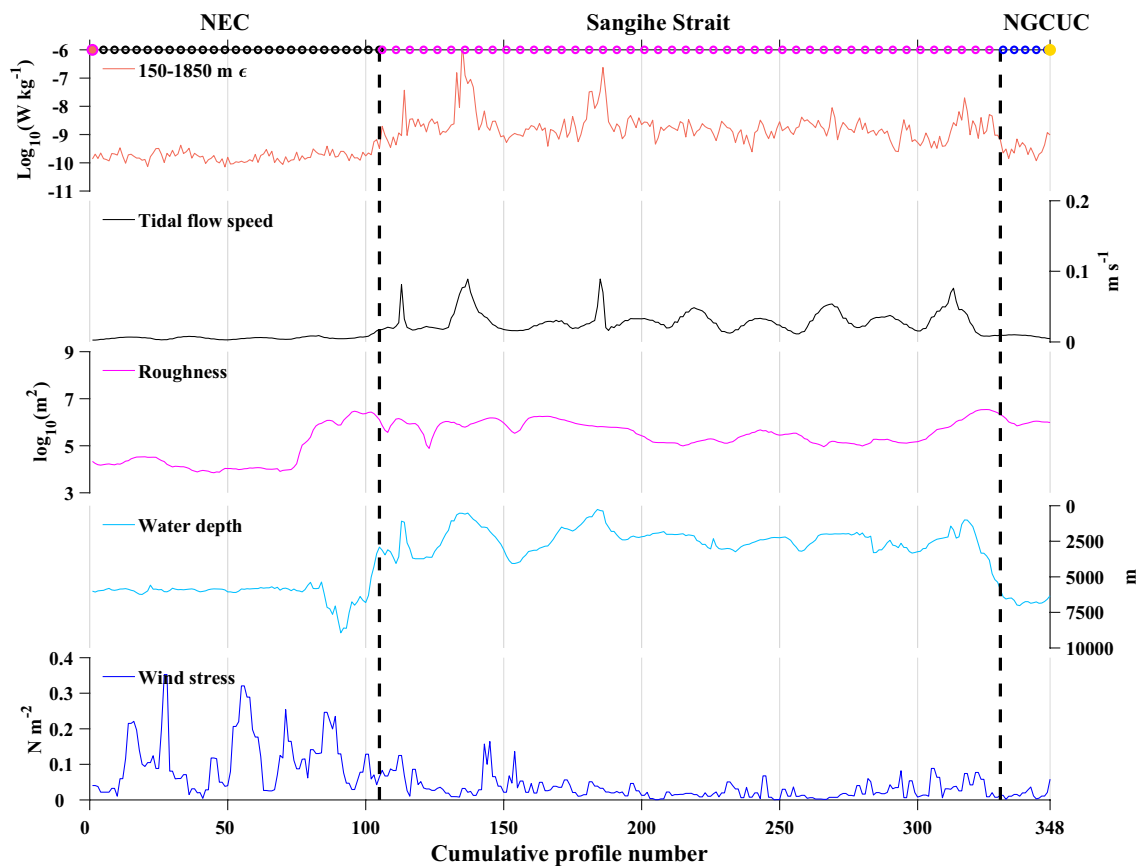
Fig. 9 Variations of dissipation rate ε averaged over a depth of 150–1850 m, the barotropic tidal flow speed, topography roughness, water depth, and wind stress along the trajectory of Argo Float 0761. The color circles on the top *x*-axes denote different regions along the trajectory of Argo Float 0761 as in Fig. 4 (color figure online)

the NPTW (24–24.5 σ_θ) and NPIW (26.5–27 σ_θ) along the trajectory of Float 2902729 are displayed in Fig. 12.

Figure 11 shows that the shape of θ–*S* diagram initially coincides with the representative θ–*S* curve of the North Pacific water masses in the NEC and WB regions, and then gradually distorts in the Sangihe Strait, and finally stops deforming in the Sulawesi Sea. The series of θ and *S* oscillate presumably due to the water mass interleaving, but the overall synchronous trend in the series of θ and *S* in each region implies the degree of water mass transformation (Fig. 12). Note that the big sudden change at the junction of the NEC region and the WB region might be associated with the missing data area mentioned in Sect. 2.1. In the Sangihe Strait, there are prominent overall trends in the series of θ and *S*, with the θ and *S* of the NPTW decreased by ~0.09 psu and ~0.40 °C, respectively, and the θ and *S* of the NPIW increased by ~0.17 psu and ~0.90 °C, respectively. Figure 5c shows that, in the Sangihe Strait, the waters above and below the isopycnals that characterize the NPTW and NPIW are mixed caused by strong diapycnal diffusivity extending throughout the observed depth.

The above analysis shows that the water masses transported by the MC have changed their characteristics before they entered the Indonesian Seas, and the water mass transformation mainly occurs in the Sangihe Strait rather than in the WB region, although there occurs strong diapycnal mixing in both regions. As mentioned in Sect. 2.1, Float 2902729 obtained 175 profiles in the Sangihe Strait but only obtained 27 profiles in the WB region, indicating much longer residence time of water masses in the Sangihe Strait than in the WB region. The drastic water mass transformation in the Sangihe Strait, therefore, may be attributed to long residence time as well as strong diapycnal mixing. It is interesting to note that the difference of the θ–*S* diagram around σ_θ = 26.5–27, for example, between stages (3) and (4) or (4) and (5) in Fig. 11 suggests that not only diapycnal mixing but also isopycnal mixing associated with the intrusion of the AAIW from the southern hemisphere play an important role in modifying the properties of the NPIW.
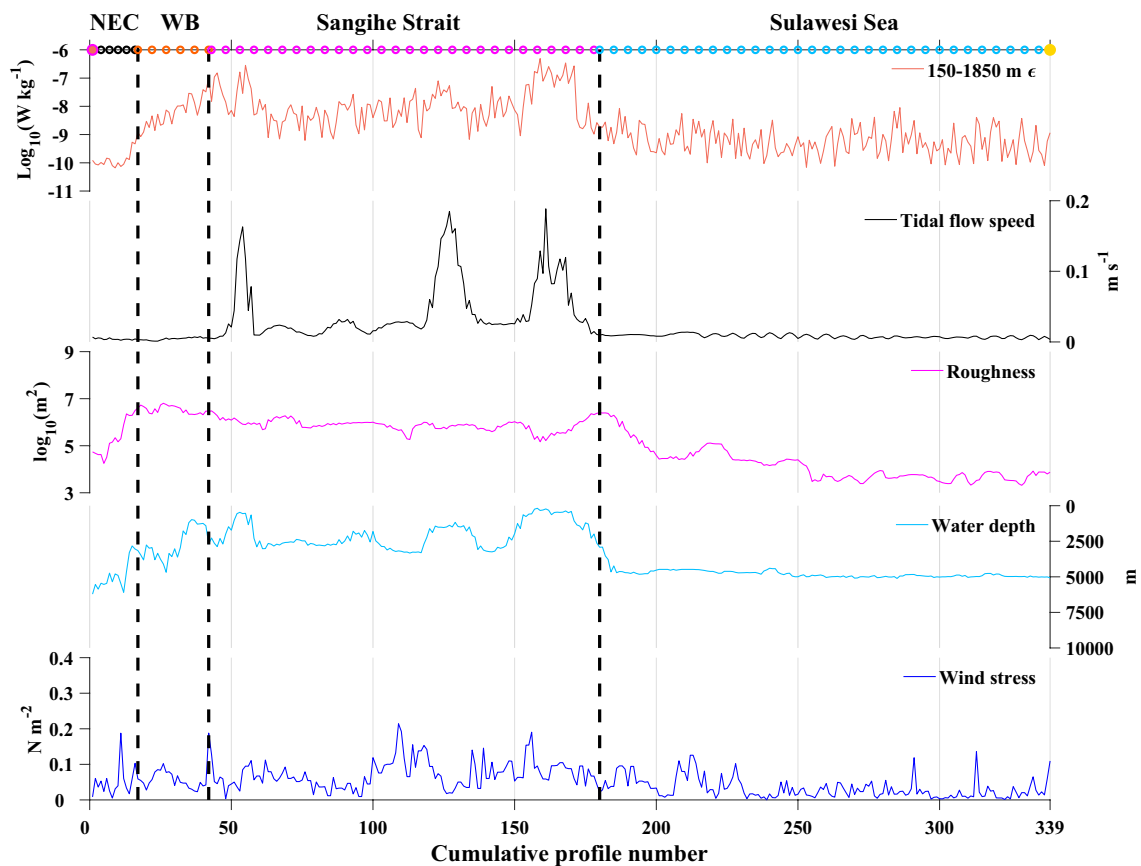
Fig. 10 As in Fig. 9 but for Argo Float 2902729

4 Summary

The Mindanao Current bridges the North Pacific low-latitude western boundary current system (NP-LLWBC) region and the Indonesian Seas by supplying the North Pacific waters to the Indonesian Throughflow (ITF). Although the previous study speculated that the diapycnal mixing along the MC might be very strong based on the water mass analysis of the gridded climatologic dataset (Li and Wang 2012), the real spatial distribution of diapycnal mixing along the MC has long remained to be clarified.

In this study, we have given the high-resolution spatial distribution of turbulent diapycnal mixing along the MC by applying strain-based finescale parameterization to the data measured by two rapid-sampling Argo floats that drifted along the MC's routes. We have found that the western boundary (WB) region close to the Mindanao Islands and the Sangihe Strait region are the two mixing hotspots along the MC, with ε and K_ρ intensified up to $\sim 10^{-6}$ W kg^{-1}

and $\sim 10^{-3}$ m^2 s^{-1}, respectively. Except for the above two mixing hotspots, the turbulent mixing along the MC is generally weak, with ε and K_ρ to be 10^{-11}–10^{-9} W kg^{-1} and 10^{-6}–10^{-5} m^2 s^{-1}, respectively. Strong mixing in the Sangihe Strait can be basically attributed to the existence of internal tides, whereas strong mixing in the WB region suggests the existence of internal lee waves, each resulting from strong tidal flow or geostrophic flow interacting with the rough bottom topography. Furthermore, through the water mass analysis of the data collected by the rapid-sampling Argo float, we have found that the water mass transformation along the MC mainly occurs in the Sangihe Strait where the water masses are subjected to strong turbulent mixing during a long residence time.

Needless to say, there remain some problems to be investigated in the future. First, the lee wave generation in the WB region can be more precisely quantified by obtaining reliable
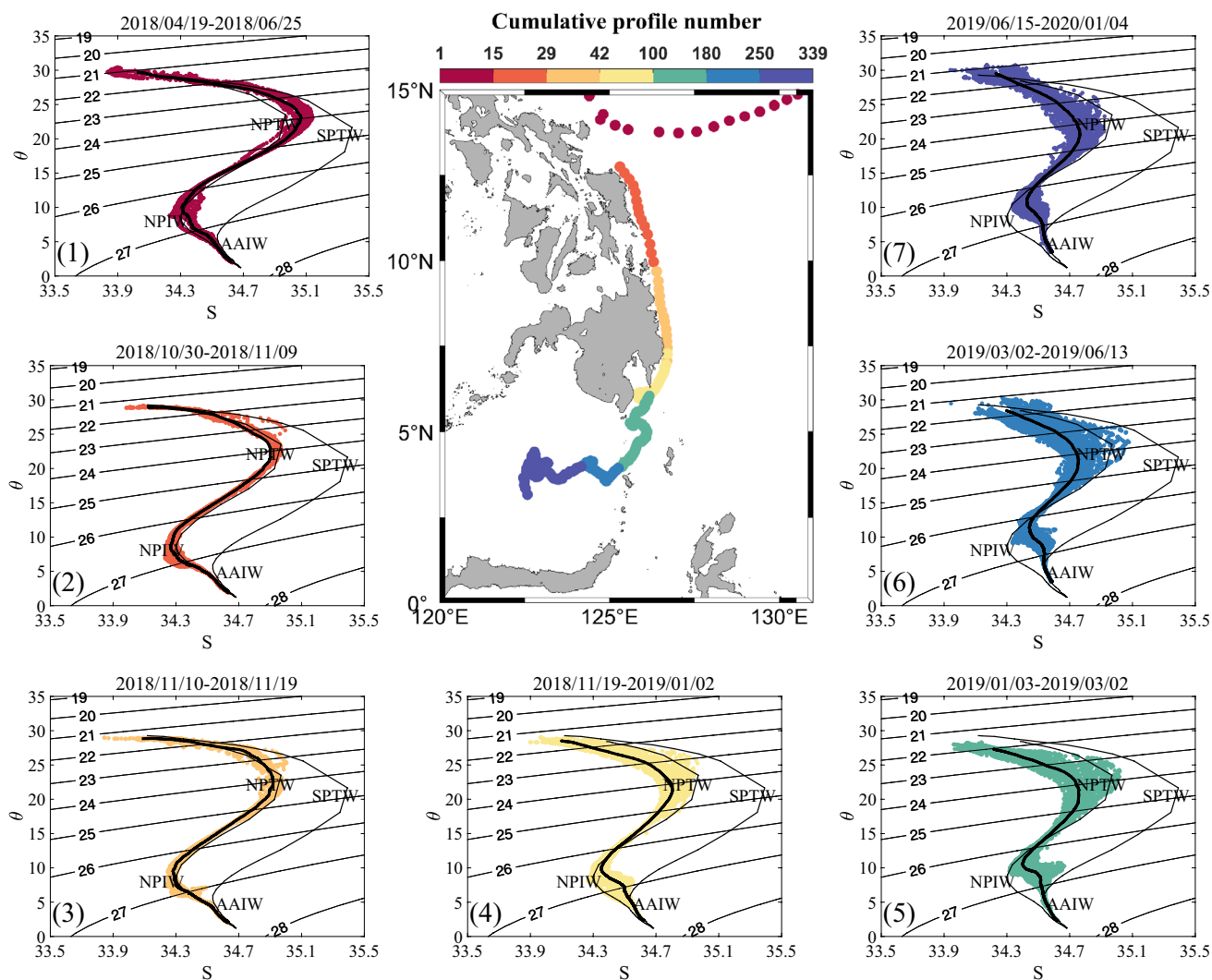
Fig. 11 θ–S diagrams obtained from Argo Float 2902729 at different locations along the MC, showing the different stages of water mass transformation. The mean θ–S curve for each stage is denoted by a bold black curve. The reference θ–S curves of the North Pacific and South Pacific water masses obtained from WOA13 annual climatology masses at 15.5° N, 130.5° E and 0°, 133° E are denoted by thin black curves

bottom velocity data. Whether or not other mechanism such as the centrifugal instability triggered by the boundary slope currents (Gula et al. 2016) is associated with turbulent mixing in the WB region can be clarified by carrying out direct microstructure measurements. Second, although our study has suggested that the water masses carried by the MC get significant transformed as they pass through the Sangihe Strait, even the effect of diapycnal mixing has not been quantitatively clarified. This remaining problem may be initiated by measuring the flow speed in the depth range of each water mass in the Sangihe Strait and applying a one-dimensional vertical diffusion equation with reference to Nagai et al. (2021).
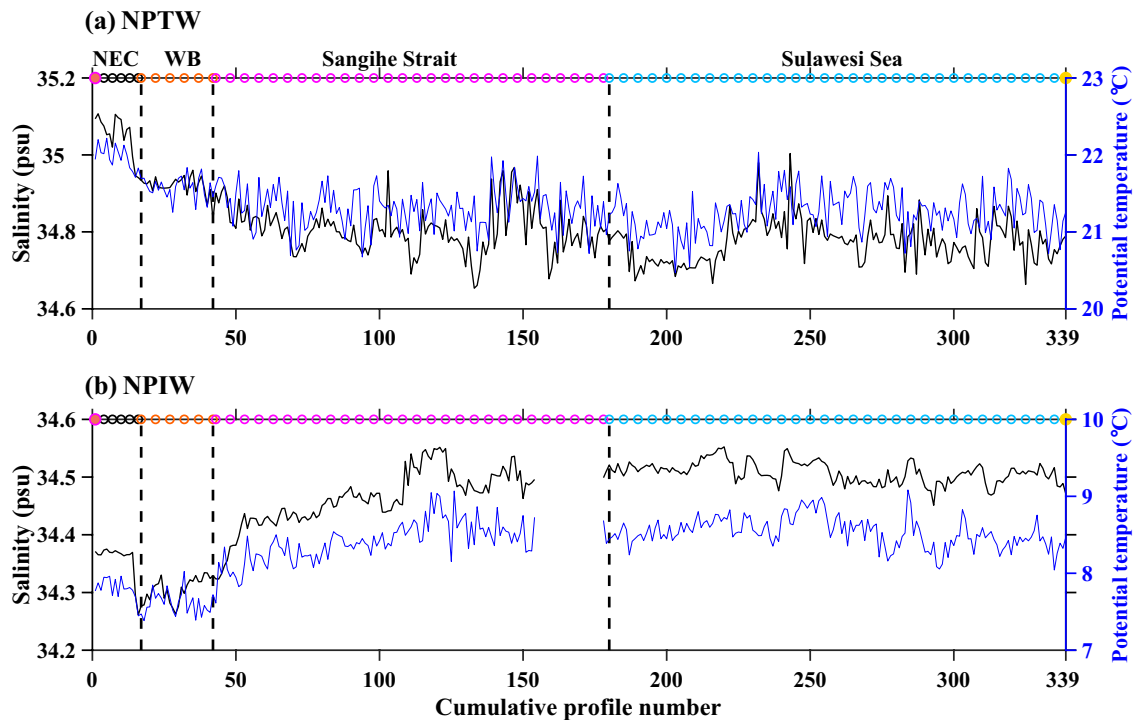
Fig. 12 Variations of potential temperature θ (blue lines) and salinity S (black lines) averaged over the isopycnals that characterize the **a** NPTW (24–24.5 σ_θ) and **b** NPIW (26.5–27 σ_θ) along the trajectory of Argo Float 2902729. The color circles on the top x-axes denote four regions along the trajectory of Argo Float 2902729 as in Fig. 5. In **b**, values of profiles 155–177 are missing due to their water depths that are shallower than the NPIW layer (color figure online)

References

Cairns JL, Williams GO (1976) Internal wave observations from a internal wave observations from a midwater float, 2. J Geophys Res Oceans 81(12):1943–1950. https://doi.org/10.1029/JC081 i012p01943

Egbert GD, Erofeeva SY (2002) Efficient inverse modeling of barotropic ocean tides. J Atmos Ocean Technol 19(2):183–204. https://doi.org/10.1175/1520-0426(2002)019%3c0183:eimobo% 3e2.0.co;2

Fine RA, Lukas R, Bingham FM, Warner MJ, Gammon RH (1994) The Western Equatorial Pacific—a water mass crossroads. J Geophys Res Oceans 99(C12):25063–25080. https://doi.org/ 10.1029/94jc02277

Firing E, Kashino Y, Hacker P (2005) Energetic subthermocline currents observed east of Mindanao. Deep Sea Res Part II Top Stud Oceanogr 52(3–4):605–613. https://doi.org/10.1016/j.dsr2. 2004.12.007

Garrett C, Kunze E (2007) Internal tide generation in the deep ocean. Annu Rev Fluid Mech 39:57–87. https://doi.org/10.1146/annur ev.fluid.39.050905.110227

Gula J, Molemaker MJ, McWilliams JC (2016) Topographic generation of submesoscale centrifugal instability and energy dissipation. Nat Commun. https://doi.org/10.1038/ncomms12811

Hibiya T, Ijichi T, Robertson R (2017) The impacts of ocean bottom roughness and tidal flow amplitude on abyssal mixing. J Geophys Res Oceans 122(7):5645–5651. https://doi.org/10.1002/ 2016jc012564

Hu DX, Cui MC, Qu TD, Li YX (1991) A subsurface northward current off Mindanao identified by dynamic calculation. Elsevier Oceanogr Ser 54:359–365

Hu D et al (2015) Pacific western boundary currents and their roles in climate. Nature 522(7556):299–308. https://doi.org/10.1038/nature14504

Kashino Y, Firing E, Hacker P, Sulaiman A (2001) Currents in the celebes and Maluku Seas. Geophys Res Lett 28(7):1263–1266. https://doi.org/10.1029/2000gl011630

Kashino Y, Ueki I, Sasaki H (2015) Ocean variability east of Mindanao: mooring observations at 7° N, revisited. J Geophys Res Oceans 120(4):2540–2554. https://doi.org/10.1002/2015jc010703

Koch-Larrouy A, Madec G, Bouruet-Aubertot P, Gerkema T, Bessieres L, Molcard R (2007) On the transformation of pacific water into Indonesian throughflow water by internal tidal mixing. Geophys Res Lett 34(4):6. https://doi.org/10.1029/2006gl028405

Koch-Larrouy A, Atmadipoera A, van Beek P, Madec G, Aucan J, Lyard F, Grelet J, Souhaut M (2015) Estimates of tidal mixing in the Indonesian archipelago from multidisciplinary INDOMIX in-situ data. Deep Sea Res Part I Oceanogr Res Pap 106:136–153. https://doi.org/10.1016/j.dsr.2015.09.007

Kunze E, Firing E, Hummon JM, Chereskin TK, Thurnherr AM (2006) Global abyssal mixing inferred from lowered ADCP shear and CTD strain profiles. J Phys Oceanogr 36(8):1553–1576. https://doi.org/10.1175/Jpo2926.1

Li YL, Wang F (2012) Spreading and salinity change of North Pacific Tropical Water in the Philippine Sea. J Oceanogr 68(3):439–452. https://doi.org/10.1007/s10872-012-0110-3

Li Y, Xu YS (2014) Penetration depth of diapycnal mixing generated by wind stress and flow over topography in the northwestern Pacific. J Geophys Res Oceans 119(8):5501–5514. https://doi.org/10.1002/2013jc009681

Liu Z, Lian Q, Zhang F, Wang L, Li M, Bai X, Wang J, Wang F (2017) Weak thermocline mixing in the North Pacific low-latitude western boundary current system. Geophys Res Lett 44(20):10530–10539. https://doi.org/10.1002/2017gl075210

Lukas R, Yamagata T, McCreary JP (1996) Pacific low-latitude western boundary currents and the Indonesian throughflow. J Geophys Res Oceans 101(C5):12209–12216. https://doi.org/10.1029/96jc01204

Nagai T, Hibiya T (2015) Internal tides and associated vertical mixing in the Indonesian Archipelago. J Geophys Res Oceans 120(5):3373–3390. https://doi.org/10.1002/2014jc010592

Nagai T, Hibiya T, Bouruet-Aubertot P (2017) Nonhydrostatic simulations of tide-induced mixing in the Halmahera sea: a possible role in the transformation of the Indonesian throughflow waters. J Geophys Res Oceans 122(11):8933–8943. https://doi.org/10.1002/2017jc013381

Nagai T, Hibiya T, Syamsudin F (2021) Direct estimates of turbulent mixing in the Indonesian Archipelago and its role in the transformation of the Indonesian throughflow waters. Geophys Res Lett. https://doi.org/10.1029/2020GL091731

Osborn TR (1980) Estimates of the local-rate of vertical diffusion from dissipation measurements. J Phys Oceanogr 10(1):83–89. https://doi.org/10.1175/1520-0485(1980)010%3c0083:Eotlro%3e2.0.Co;2

Polzin KL, Garabato ACN, Huussen TN, Sloyan BM, Waterman S (2014) Finescale parameterizations of turbulent dissipation. J Geophys Res Oceans 119:1383–1419. https://doi.org/10.1002/2013JC008979

Sheen KL et al (2013) Rates and mechanisms of turbulent dissipation and mixing in the Southern Ocean: results from the diapycnal and isopycnal mixing experiment in the Southern Ocean (DIMES). J Geophys Res Oceans 118(6):2774–2792. https://doi.org/10.1002/jgrc.20217

Smith WHF, Sandwell DT (1997) Global sea floor topography from satellite altimetry and ship depth soundings. Science 277(5334):1956–1962. https://doi.org/10.1126/science.277.5334.1956

Wang F et al (2016) Semiannually alternating exchange of intermediate waters east of the Philippines. Geophys Res Lett 43(13):7059–7065. https://doi.org/10.1002/2016gl069323

Whalen CB, MacKinnon JA, Talley LD, Waterhouse AF (2015) Estimating the mean diapycnal mixing using a finescale strain parameterization. J Phys Oceanogr 45(4):1174–1188. https://doi.org/10.1175/jpo-d-14-0167.1

Winkel DP, Gregg MC, Sanford TB (2002) Patterns of shear and turbulence across the Florida Current. J Phys Oceanogr 32(11):3269–3285. https://doi.org/10.1175/1520-0485(2002)032%3c3269:posata%3e2.0.co;2

Yang QX, Zhao W, Li M, Tian JW (2014) Spatial structure of turbulent mixing in the Northwestern Pacific Ocean. J Phys Oceanogr 44(8):2235–2247. https://doi.org/10.1175/Jpo-D-13-0148.1

Yuan D et al (2018) Observed transport variations in the Maluku Channel of the Indonesian Seas associated with western boundary current changes. J Phys Oceanogr 48(8):1803–1813. https://doi.org/10.1175/jpo-d-17-0120.1

Zhu YC, Zhang RH (2018) An argo-derived background diffusivity parameterization for improved ocean simulations in the Tropical Pacific. Geophys Res Lett 45(3):1509–1517. https://doi.org/10.1002/2017gl076269